

**Formation of the rare-earth peak: Gaining insight into late-time  $r$ -process dynamics**Matthew R. Mumpower<sup>\*</sup> and G. C. McLaughlin<sup>†</sup>*Department of Physics, North Carolina State University, Raleigh, North Carolina 27695-8202, USA*Rebecca Surman<sup>‡</sup>*Department of Physics and Astronomy, Union College, Schenectady, New York 12308, USA*

(Received 21 September 2011; revised manuscript received 21 November 2011; published 2 April 2012)

We study the formation and final structure of the rare-earth peak ( $A \sim 160$ ) of the  $r$ -process nucleosynthesis. Under high-entropy conditions ( $S > 100k_B$ ), the rare-earth peak forms at late times in the  $r$ -process after neutron exhaustion (neutron-to-seed ratio  $R = 1$ ) as matter decays back to stability. Since rare-earth peak formation does not occur during  $(n, \gamma) \rightleftharpoons (\gamma, n)$  equilibrium it is sensitive to the strong interplay between late-time thermodynamic evolution and nuclear physics input. Depending on the conditions, the peak forms either because of the pattern of the neutron capture rates or because of the pattern of the separation energies. We analyze three nuclear data sets under different thermodynamic conditions. We find that the subtleties of each nuclear data set, including separation energies and neutron capture rates, influence not only the final shape of the peak but also when it forms. We identify the range of nuclei which are influential in rare-earth peak formation.

DOI: [10.1103/PhysRevC.85.045801](https://doi.org/10.1103/PhysRevC.85.045801)

PACS number(s): 26.30.Hj, 26.50.+x

**I. INTRODUCTION**

Approximately half of the elements beyond  $A = 100$  are made in the “rapid” neutron capture process, or  $r$ -process, in which successive neutron captures occur on time scales faster than  $\beta$  decays. The elements in the range  $80 < A < 100$  might also be synthesized this way. At the present time, there is significant uncertainty regarding the astrophysical environment responsible for this synthesis event [1,2]. The leading candidate site [3] is believed to be core-collapse supernovae (e.g., [4–10]), even though most recent simulations do not yield favorable conditions for the  $r$ -process [11–13]. Other candidate sites include compact object mergers [14–21],  $\gamma$ -ray burst outflows [22–24], neutrino-induced nucleosynthesis in He shells [25,26], supernova fallback [27], and collapse of O-Ne-Mg cores [28–30].

Experimentally, it is difficult to measure the properties of the short-lived nuclei far from stability that participate in the  $r$ -process. Recent developments using radioactive beams show promise (e.g., [31,32]), but current experimental data on neutron-rich isotopes are limited. Thus  $r$ -process studies must rely not only on model calculations of the environment but also on theoretical nuclear models (e.g., [33–35]).

Despite these difficulties, much has been learned about the  $r$ -process over the past 50 years. The most prominent features in the  $r$ -process abundance distribution above atomic mass number of  $A = 100$  are two distinct peaks occurring at  $A = 130$  and  $A = 195$ . It was hypothesized very early that the formation of these peaks should be associated with the long  $\beta$ -decay rates of closed neutron shells [36]. Since this seminal paper, much effort has been put into researching the conditions for a sufficient initial neutron-to-seed ratio, a key requirement

in order to produce a “main”  $r$ -process out to the third peak ( $A = 195$ ). For reviews see [1,2,37,38].

After the two main peaks, the second most prominent feature above  $A = 100$  is the smaller peak near  $A \sim 160$  known as the rare-earth peak. While less abundant than the other peaks, the rare-earth peak can in principle be used as a powerful tool and offers an alternative way to probe the  $r$ -process. This is due to the following properties: (1) Observational data from metal-poor stars show very consistent trends among the rare-earth and heavier elements. This suggests that these elements were created in the same type of synthesis event [39]. Thus, the rare-earth peak provides a natural diagnostic of  $r$ -process models. (2) The rare-earth peak forms away from closed neutron or proton shells in freeze-out when a conducive pattern exists in separation energies or neutron capture rates. This is in contrast to the  $A = 130$  and  $A = 195$  peaks which form from a combination of long  $\beta$ -decay rates and other nuclear properties at closed shells. Thus, the rare-earth peak is a different and unique probe of late-time  $r$ -process conditions. (3) The rare-earth peak is extremely sensitive not only to late-time thermodynamic behavior but also to nuclear physics input [40–42]. Typical variations in final rare-earth abundance patterns from simulations with different nuclear models are highlighted in Fig. 1.

To date the rare-earth region has received relatively little attention. Fission cycling has been suggested as a mechanism for obtaining the rare-earth peak [43,44], but it is not favored, as reported in Ref. [45]. Large uncertainties found in fission probabilities and fragment distributions of current nuclear models further compound difficulties with a successful description of rare-earth peak formation by fission cycling [19]. Surman *et al.* [40] investigated the formation of the peak in a hot  $r$ -process environment with temperatures high enough to support  $(n, \gamma) \rightleftharpoons (\gamma, n)$  equilibrium. The formation of the rare-earth peak under these conditions was attributed to the co-action of nuclear deformation and  $\beta$  decay as the free neutrons are quickly captured during freeze-out. This was

<sup>\*</sup>mrmumpow@ncsu.edu<sup>†</sup>gail\_mclaughlin@ncsu.edu<sup>‡</sup>surmanr@union.edu

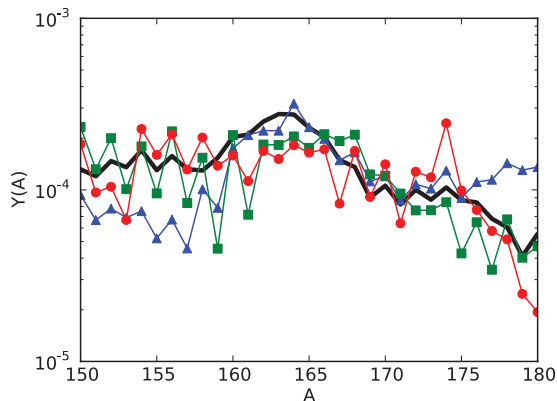


FIG. 1. (Color online) The resultant rare-earth peaks from simulations with nuclear models FRDM [33] (blue triangles), ETFSI-Q [34] (green squares), and HFB-17 [35] (red circles) along with the solar  $r$ -process abundance pattern ( $N_{\odot,r}$  versus atomic mass) (data from [71]). The same colors and geometric markers for each nuclear model will be used in the remaining figures.

followed by a study of late-time abundance changes among the major peaks [46]. Otsuki *et al.* [47] investigated a range of  $r$ -process models and found similar rare-earth elemental abundance patterns, provided the temperature was constant during freeze-out. Most recently, Arcones *et al.* [42] studied the sensitivity of late-time abundance fluctuations to changes in the nuclear physics inputs. Arcones *et al.* [42] pointed out that the rare-earth peak is sensitive to changes at late times, e.g., to nonequilibrium effects such as neutron capture, even when the abundance of free neutrons can become very low ( $\sim 10^{-5}$ ).

This paper presents a more complete picture of rare-earth peak formation under high-entropy conditions,  $S > 100k_B$ . We explore the sensitivity of the peak formation mechanism to late-time thermodynamic behavior and nuclear physics input. The “funneling” formation mechanism of [40] is reviewed for hot evolutions. We introduce a different “trapping” mechanism for peak formation in cold evolutions where the temperatures and densities decline relatively quickly and therefore photodissociation plays no role in the late-time dynamics after  $R = 1$ . We study the effects of three different nuclear models and show how large uncertainties in this region stem from nuclear physics. Lastly, we show that the nuclei which contribute to peak formation are approximately 10 to 15 neutrons from stability and thus represent prime candidates to be measured in future radioactive ion beam facilities (the Facility for Rare Isotope Beams [48] or the GSI Facility for Antiproton and Ion Research [49]).

## II. $r$ -PROCESS CONDITIONS AND CALCULATIONS

Abundance-weighted lifetimes are used throughout the text to characterize the late-time dynamics of the  $r$ -process. These are provided below for the reader’s convenience:

$$\tau_{n\gamma} \equiv \frac{\sum_{Z \geq 8, A} Y(Z, A)}{\sum_{Z \geq 8, A} N_n \langle \sigma v \rangle_{Z, A} Y(Z, A)}, \quad (1a)$$

$$\tau_{\gamma n} \equiv \frac{\sum_{Z \geq 8, A} Y(Z, A)}{\sum_{Z \geq 8, A} \lambda_{\gamma n}(Z, A) Y(Z, A)}, \quad (1b)$$

$$\tau_{\beta} \equiv \frac{\sum_{Z \geq 8, A} Y(Z, A)}{\sum_{Z \geq 8, A} \lambda_{\beta}(Z, A) Y(Z, A)}, \quad (1c)$$

where  $N_n$  is the neutron number density,  $\langle \sigma v \rangle_{Z, A}$  is the thermally averaged neutron capture cross section for nuclei  $(Z, A)$ ,  $\lambda_{\gamma n}(Z, A)$  is the photodissociation rate for nuclei  $(Z, A)$ ,  $\lambda_{\beta}(Z, A)$  is the full  $\beta$ -decay rate (including  $\beta$ -delayed neutron emission channels) for nuclei  $(Z, A)$ , and  $Y(Z, A)$  is the abundance of nuclei  $(Z, A)$ . A reduced sum denoted with a superscript “REP” is taken over the rare-earth region,  $A = 150$  to  $A = 180$ , when applicable. The neutron-to-seed ratio or  $R$  is defined as

$$R \equiv \frac{Y_n}{\sum_{Z \geq 8, A} Y(Z, A)}, \quad (2)$$

where  $Y_n$  is the abundance of free neutrons.

Since rare-earth peak formation is highly dependent on the rate of decrease in the temperature and density, we consider rare-earth peak formation under two different thermodynamic evolutions. One scenario is a classical “hot”  $r$ -process, which operates under high temperatures ( $T_9 \gtrsim 1$ ) at the time in which neutron captures are important for peak formation. A second scenario is a “cold”  $r$ -process, which operates under low temperatures ( $T_9 \sim 0.5$ ) at the time in which neutron captures are important for peak formation [50]. We note that the hot and cold terminology does not refer to the entropy, but instead it signifies the differences in the conditions as the  $r$ -process nuclides fall out of  $(n, \gamma) \rightleftharpoons (\gamma, n)$  equilibrium. This distinction is critical to determining the important reaction channels during freeze-out. We briefly discuss this below.

The classical  $r$ -process begins with a phase of  $(n, \gamma) \rightleftharpoons (\gamma, n)$  equilibrium marked by an abundance-weighted lifetime ratio of neutron capture to photodissociation of  $\tau_{n\gamma}/\tau_{\gamma n} = 1$ . During this phase the temperature is still sufficiently high so that neutron captures dominate  $\beta$  decays ( $\tau_{\beta}/\tau_{n\gamma} \gg 1$ ) and the Saha equation can be used to determine abundances along an isotopic chain [38].

The second phase, known as the freeze-out epoch, is marked by the weakening of the  $(n, \gamma) \rightleftharpoons (\gamma, n)$  equilibrium ( $\tau_{n\gamma}/\tau_{\gamma n} \lesssim 1$ ) and the abundance-weighted lifetime ratio of  $\beta$  decay versus neutron capture falls to  $\tau_{\beta}/\tau_{n\gamma} \approx 1$ . It is during this phase that the formation of the rare-earth peak proceeds with competition among neutron captures, photodisintegrations, and  $\beta$  decays.

In the cold  $r$ -process the first phase  $(n, \gamma) \rightleftharpoons (\gamma, n)$  equilibrium is dramatically shorter than the first phase of the classical scenario. Freeze-out is now caused by a rapid drop in temperature and/or density rather than the consumption of free neutrons (as in the classical case). The bulk of the cold  $r$ -process operates in the second phase, under low temperatures ( $T_9 \sim 0.5$ ), where photodisintegrations have frozen out [50].

Once neutron exhaustion ( $R = 1$ ) occurs in the cold  $r$ -process the free neutrons available to the system must come from the recapture of  $\beta$ -delayed emitted neutrons. The importance of this effect on the final abundance distribution

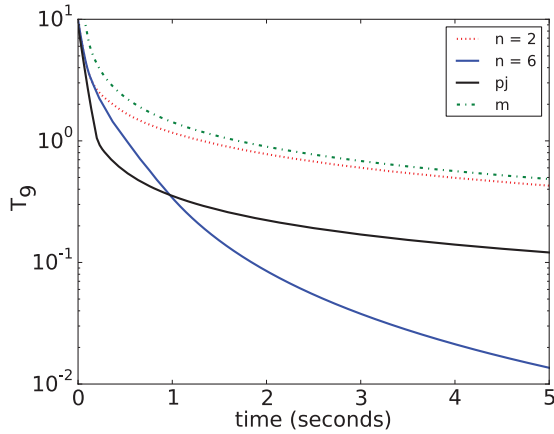


FIG. 2. (Color online) Temperature evolutions for our parameterized outflows ( $n = 2$  and  $n = 6$ ) and two other evolutions (m and pj). The rare-earth peak forms in each evolution.

was noted in Refs. [42,51]. This recapture effect is crucial to peak formation, as can be seen from the fact that malformed abundance distributions result if  $\beta$ -delayed neutron emission is artificially turned off (see Ref. [42]).

Our calculations consist of a nuclear reaction network containing  $r$ -process-relevant nuclides as described in Refs. [40,46]. Previous versions of this network code have been used in the studies of Beun [52] and Surman [53]. The primary reaction channels for nuclides in this section of the reaction network are  $\beta$  decay, neutron capture, and photodissociation. Our fully implicit  $r$ -process reaction network handles consistently neutron capture rates at low temperatures and calculations with low abundances of free neutrons, both important for simulations with cold evolutions. For the initial abundances we use self-consistent output from an intermediate reaction network [54] with the PARDISO solver [55].

Our  $r$ -process calculations start at  $T_9 = 2$  with densities  $\rho \approx 0.9 \times 10^4 \text{ g/cm}^3$  for hot evolutions with entropy per baryon of  $S = 200$  in units of Boltzmann's constant and electron fraction  $Y_e = 0.30$  and with  $\rho \approx 0.5 \times 10^4 \text{ g/cm}^3$  for cold evolutions with  $S = 300$  and  $Y_e = 0.40$ . Before  $T_9 = 2$  our calculations evolve with time scale  $\tau = 80 \text{ ms}$ . The range of time scales,  $\tau$ , which are conducive to rare-earth peak formation can be seen in Fig. 1 of [41] for both hot and cold  $r$ -process evolutions. At  $T_9 = 2$ , the neutron-to-seed ratios are  $R \approx 45$  and  $R \approx 35$ , respectively. We study the late-time hot and cold  $r$ -process evolutions in the context of a monotonically

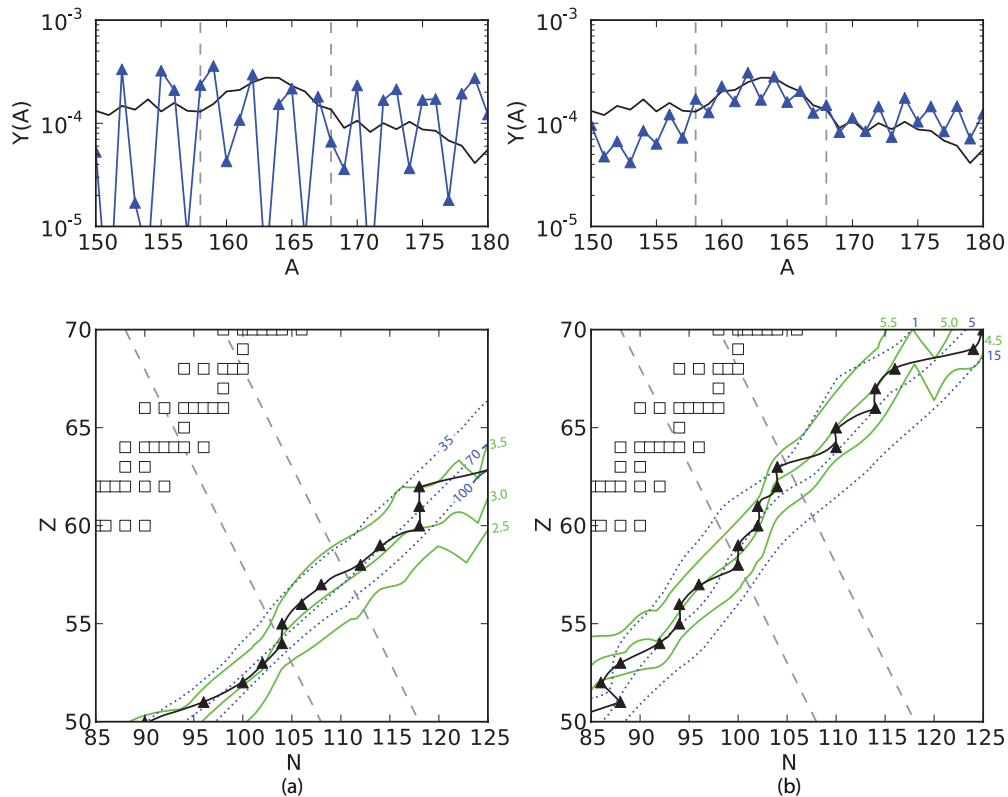


FIG. 3. (Color online) Plots showing how the rare-earth peak forms under hot environments when the  $r$ -process path encounters the kink in the separation energies. Panels (a) and (b) each show a snapshot of an abundance pattern along with separation energies (MeV),  $\beta$ -decay rates ( $\text{s}^{-1}$ ), and  $r$ -process path from a simulation with the FRDM nuclear model. Panel (a) show a snapshot at neutron exhaustion,  $R = 1$ . Panel (b) show a snapshot of the  $r$ -process path beginning to move closer to stability while the peak forms. Connected black triangles represent the  $r$ -process path. Dotted blue lines represent constant total  $\beta$ -decay rate for even- $N$  nuclei. Solid green lines represent constant separation energy for even- $N$  nuclei. Faint diagonal dotted lines delineate the borders of the peak region ( $A = 159$  to  $A = 167$ ). Stable isotopes are shown by unfilled squares.

decreasing temperature with density parametrized as

$$\rho(t) = \rho_1 \exp(-t/\tau) + \rho_2 \left( \frac{\Delta}{\Delta + t} \right)^n, \quad (3)$$

where  $\rho_1 + \rho_2$  is the density at time  $t = 0$ ,  $3\tau = \tau_{\text{dyn}}$ ,  $\Delta$  is a constant real number, and  $n$  controls the type of late-time  $r$ -process evolution (the time when rare-earth peak formation occurs). The early-time behavior of the outflow is dominated by the first term on the right-hand side while the late-time behavior is dominated by the second term. For hot  $r$ -process evolutions we set  $n = 2$  and for cold  $r$ -process evolutions we set  $n = 6$ . A decaying density of  $n = 2$  is characteristic of wind models [56,57] at late times while  $n = 6$  represents a faster decline.

We show in Fig. 2 the temperature as a function of time for our evolutions ( $n = 2$  and  $n = 6$ ) and two other evolutions “m” [56] and “pj” [57] previously used in the literature as hot and cold  $r$ -process scenarios, respectively. In each case the temperature is calculated self-consistently by assuming constant entropy [58]. The rare-earth peak forms by the hot mechanism in the  $n = 2$  and “m” evolutions and by the cold mechanism in both  $n = 6$  and “pj” evolutions.

We use three different nuclear data sets in our nucleosynthesis calculations: the finite-range droplet model (FRDM)

[33], the extended Thomas-Fermi with Strutinsky integral and quenching data set (ETFSI-Q) [34], and version 17 of the Hartree-Fock-Bogoliubov masses (HFB-17) [35]. The FRDM and ETFSI-Q neutron capture rates are from [59] and were computed with the statistical model code NON-SMOKER [60]. The HFB-17 neutron capture rates are from the publicly available Brusslib online database [61] and were computed with the statistical model code TALYS [62], which is also publicly available. The HFB nuclear model is under constant development and is therefore updated with the latest experimental data and theoretical techniques [63]. The  $\beta$ -decay rates used in our  $r$ -process network come from [64].

### III. PEAK FORMATION IN HOT ENVIRONMENTS

The mechanism for rare-earth peak formation in hot environments was first described in Ref. [40]. We review the basic physical arguments in this section.

Under hot conditions the  $r$ -process path (time ordered set of most abundant isotopes) traverses the  $NZ$  plane between the line of stability and the neutron drip line. The path is initially constrained by  $(n, \gamma) \rightleftharpoons (\gamma, n)$  equilibrium and is thus found to lie on a line of constant separation energy via the Saha equation. As the free neutrons are consumed, the path moves

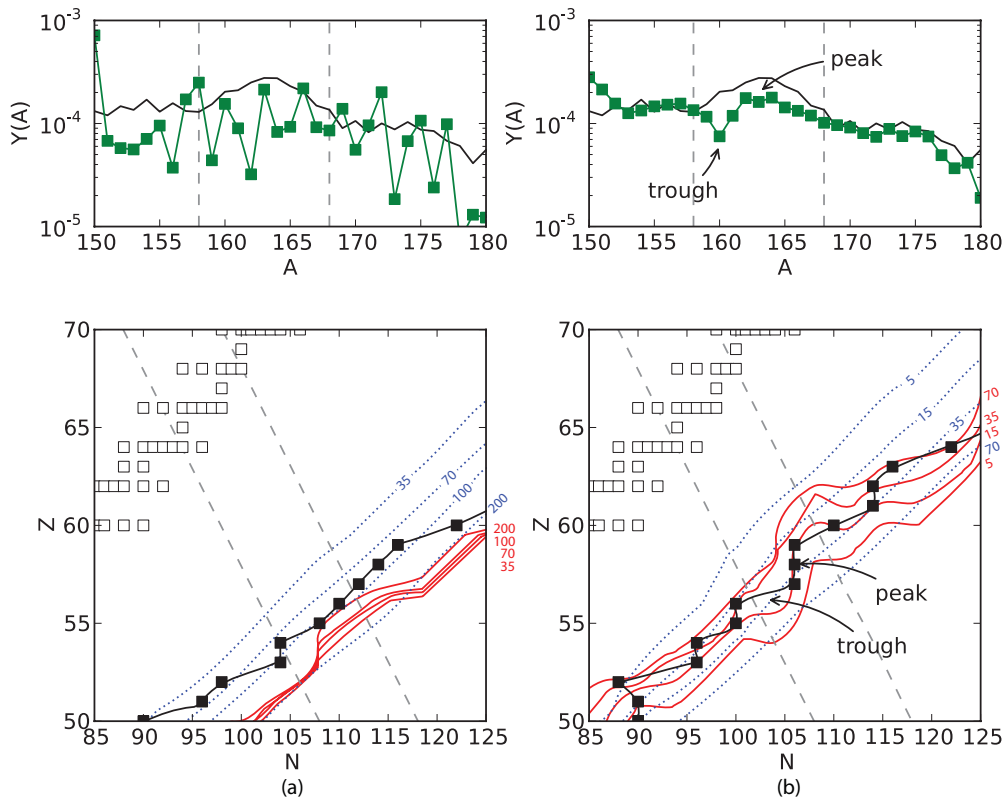


FIG. 4. (Color online) Plots showing how the rare-earth peak forms under cold environments when the  $r$ -process path encounters slower neutron capture rates in the peak region. Panels (a) and (b) each show a snapshot of an abundance pattern along with neutron capture rates ( $s^{-1}$ ),  $\beta$ -decay rates ( $s^{-1}$ ), and  $r$ -process path from a simulation with the ETFSI-Q nuclear model. Panel (a) show a snapshot just after neutron exhaustion,  $R = 1$ . Panel (b) show a snapshot of the abundance pattern and rates as the  $r$ -process path begins to move closer to stability and the peak begins to form. Connected black squares represent the  $r$ -process path and red lines represent constant neutron capture rates for even- $N$  nuclei. All other markers are the same as in Fig. 3.

back toward stability and  $(n, \gamma) \rightleftharpoons (\gamma, n)$  equilibrium begins to break down. During this freeze-out from equilibrium, rare-earth peak formation can potentially occur. In our calculations we determine the location of the  $r$ -process path by computing an abundance-weighted average over isotopic chains.

The necessary and sufficient conditions for peak formation are as follows: (1) a deformation maximum or other nuclear structure effect must produce a kink in the lines of constant neutron separation energy around  $A \sim 160$ , and (2) the  $r$ -process path must traverse this kink region during freeze-out, before  $\beta$  decay takes over in the region. The latter allows for the interplay of neutron capture, photodissociation, and  $\beta$  decay as the  $r$ -process path crosses the region which contains the separation energy kink.

During peak formation, the  $r$ -process path moves toward stability at a rate approximately equal to the average  $\beta$ -decay rate along the path. The separation energy kink causes a corresponding kink in the  $r$ -process path as material moves through this important region. This provides a mismatch between the  $\beta$ -decay rates of material below and above the kink. Due to the kink in the path, nuclei below the peak ( $A = 150$  to  $A = 158$ ) are farther from stability and so  $\beta$ -decay faster than the average nuclei along the path. Since

the nuclei below the peak decay faster than the path moves, these nuclei then proceed to capture neutrons in an attempt to return the  $r$ -process path back to equilibrium. Conversely, due to the kink in the path, nuclei above the peak ( $A = 168$  to  $A = 180$ ) are closer to stability and so  $\beta$ -decay slower than average along the path. The path therefore moves before these nuclei have a chance to decay and so they photodissociate to shift the  $r$ -process path back to equilibrium. In the peak region ( $A = 159$  to  $A = 167$ ) some nuclei are still in  $(n, \gamma) \rightleftharpoons (\gamma, n)$  equilibrium, which limits the amount of material flowing out of the peak region in either direction. The net result causes material to funnel into the peak region, creating the local maximum.

The essence of this effect is shown in Fig. 3. At neutron exhaustion,  $R = 1$  (left panels), the  $r$ -process is just beginning to break from  $(n, \gamma) \rightleftharpoons (\gamma, n)$  equilibrium. Here the path lies along a line of constant separation energy ( $\sim 3.0$  MeV) and the abundances show an odd-even effect due to the population of primarily even- $N$  nuclei in equilibrium. No peak exists at this time.

Later in the simulation (right panels), peak formation occurs as the path encounters the region with the separation energy kink. The separation energy kink causes the kink in the

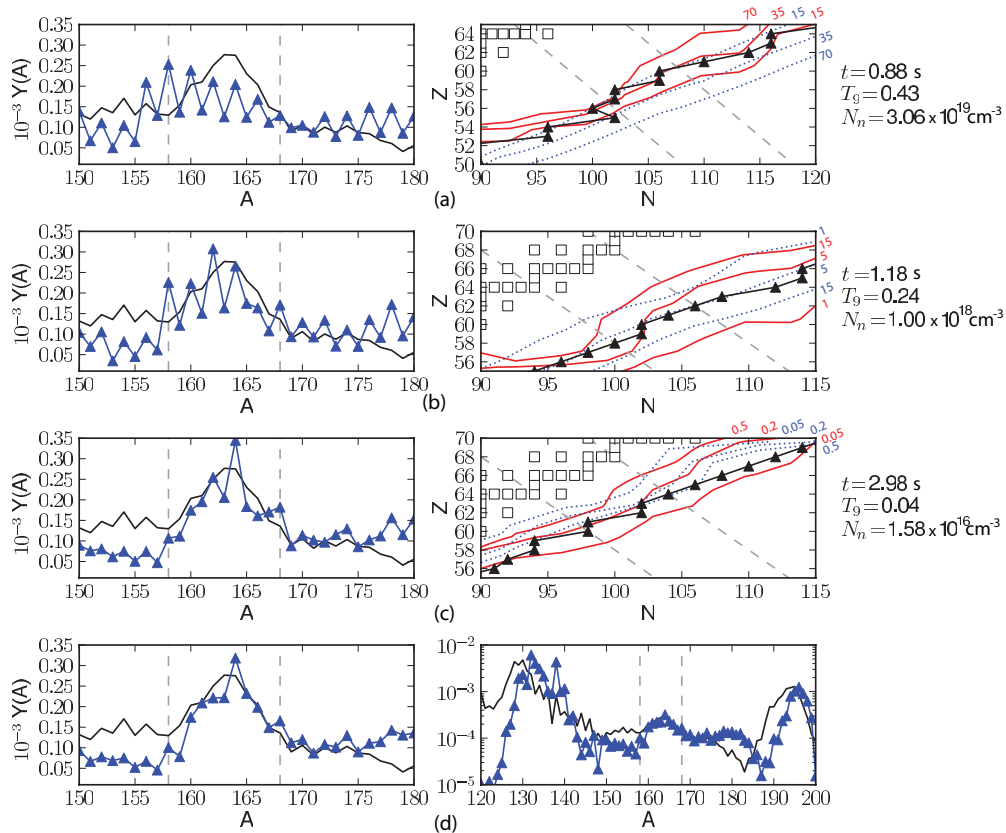


FIG. 5. (Color online) A successful rare-earth peak formation under a cold evolution with FRDM nuclear data occurs when the structure in the neutron capture rates lasts all the way to stability. The structure in the neutron capture rates is not yet present at 20 neutrons away from stability (a). However, the structure in the neutron capture rates becomes evident when the path is 15 neutrons away from stability (b), continuing until the abundance pattern has frozen out completely. Neutron capture rates (solid red lines),  $\beta$ -decay rates (dotted blue lines),  $r$ -process path (filled squares in the right-column plots) and abundance snapshots (left column) are shown at (a) 20, (b) 15, and (c) 10 neutrons away from stability. In panel (d) the final abundances are shown.

$r$ -process path. Nuclei along the path in the peak region have  $\beta$ -decay rates which range from  $1 \text{ s}^{-1}$  (above the kink) to  $10 \text{ s}^{-1}$  (below the kink). The resultant photodissociation above the kink and  $\beta$ -decay followed by neutron capture below the kink causes material to funnel into the peak region.

#### IV. PEAK FORMATION IN COLD ENVIRONMENTS

In the previous section we analyzed rare-earth peak formation in hot evolutions and found that photodissociation was crucial in peak formation. However, we also find well-formed solar-like rare-earth peaks in simulations of cold environments where photodissociation plays no role in the dynamics after  $R = 1$ .

After  $R = 1$ , the cold  $r$ -process path is controlled on average by the competition between neutron captures and  $\beta$  decays,  $\tau_\beta/\tau_{n\gamma} \approx 1$ . Locally, over the rare-earth region, the exact position of the path is more complicated due to the variation among individual rates.

As the material decays back to stability, peak formation will ensue if the path encounters a peak region where neutron capture rates are slow relative to the above and below regions. The essence of the effect is that slow neutron capture rates

in the peak region cause a bow (inward toward stability) in the lines of constant neutron capture rates relative to the lines of constant  $\beta$ -decay rates, thus causing material to become trapped in the peak region.

The cold formation mechanism is shown in Fig. 4. The left panels show a snapshot of the abundance pattern and rates at neutron exhaustion,  $R = 1$ . At this point in time the  $r$ -process path is still influenced by residual photodissociation flows. This is reflected in an odd-even effect in the abundances and flat  $r$ -process path (similar to hot evolutions). However, the photodissociation rates are decreasing so rapidly that they play no further role in the dynamics after this point. Shortly, the neutron capture rates will become comparable to the  $\beta$ -decay rates and large odd-even behavior of the abundances will be washed out [65]. In fact, this has already begun to happen, as can be seen with the slight bowing of the neutron capture rate lines in the peak region ( $A = 159$  to  $A = 167$ ).

At a slightly later time in the simulation (right panels of Fig. 4) the system has moved closer to stability and the  $r$ -process path now encounters the slower capture rates in the peak region. Below the peak ( $A = 150$  to  $A = 158$ ), neutron captures occur much faster than  $\beta$ -decay rates along the  $r$ -process path, so the net result is material shifting toward

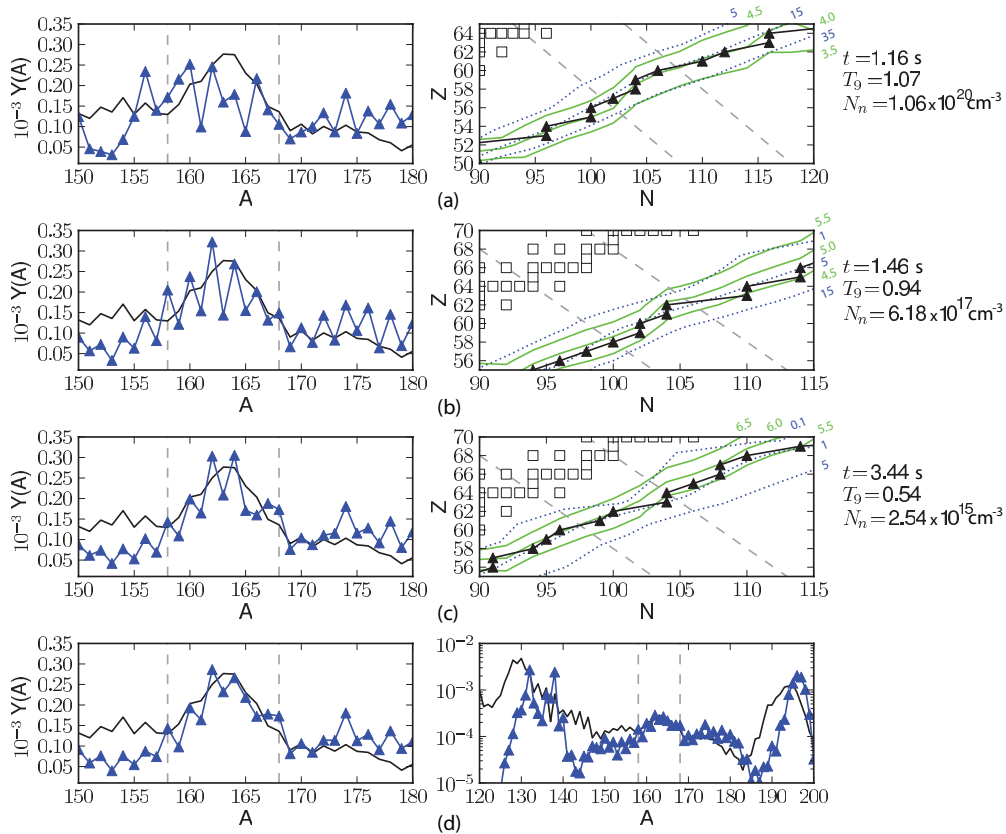


FIG. 6. (Color online) A successful rare-earth peak formation under a hot evolution with FRDM nuclear data. The  $r$ -process path encounters the well-defined separation energy kink between 20 and 15 neutrons away from stability in the peak region; see panels (a) and (b). The separation energy kink does not last (c), but by this time  $\beta$  decays have taken over and the abundances have nearly frozen out. Separation energies (solid green lines),  $\beta$ -decay rates (dotted blue lines),  $r$ -process path (filled triangles in the right column), and abundance snapshots (left column) are shown at (a) 20, (b) 15, and (c) 10 neutrons away from stability. In panel (d) the final abundances are shown.

the peak region. In the peak region the path encounters the slow capture rates (note the bowing of the neutron capture rate lines) so that any material being shifted into the peak region becomes hung up. Above the peak ( $A = 168$  to  $A = 180$ ), the flow of material is again dominated by the relatively faster neutron capture rates. The net result is trapping of material into the peak region.

Another interesting feature found when using this set of nuclear data in the right panel of Fig. 4 is the trough to the left of the peak. A trough can occur if a gap in the  $r$ -process path proceeds for long periods of time as matter decays back to stability. Along a gap in the  $r$ -process path the neutron capture rates are relatively fast, resulting in movement of material to more neutron rich isotopes and a depletion of material in the gap region.

In our figures, the lines of constant neutron capture rates have been averaged over even- $N$  nuclei. Even- $N$  neutron capture rates are more important to rare-earth peak formation because, at a given temperature, odd- $N$  nuclei have faster neutron capture rates, which causes material to pass through the odd- $N$  nuclei quickly. Thus material builds up (or stays) in even- $N$  nuclei, which sets the  $r$ -process path. The importance

of individual neutron capture rates in the rare-earth peak was highlighted in Ref. [41].

## V. INFLUENCE OF NUCLEAR DATA ON RARE-EARTH PEAK FORMATION

From the previous two sections it is clear that the details of the late-time thermodynamic evolution are critical in setting the relevant nuclear physics and thus determine the mechanism for peak formation.

Despite the differences in peak formation mechanisms, we find that the final abundances among simulations with the same nuclear data yet differing late-time thermodynamic behavior can be remarkably similar. This is in contrast to the differences found in the final abundance pattern when comparing nuclear data sets with similar thermodynamic conditions. In this section we focus on the influence of different separation energies and neutron capture rates on rare-earth peak formation.

A successful peak formation is imprinted on the final abundances in a cold evolution when the  $r$ -process path

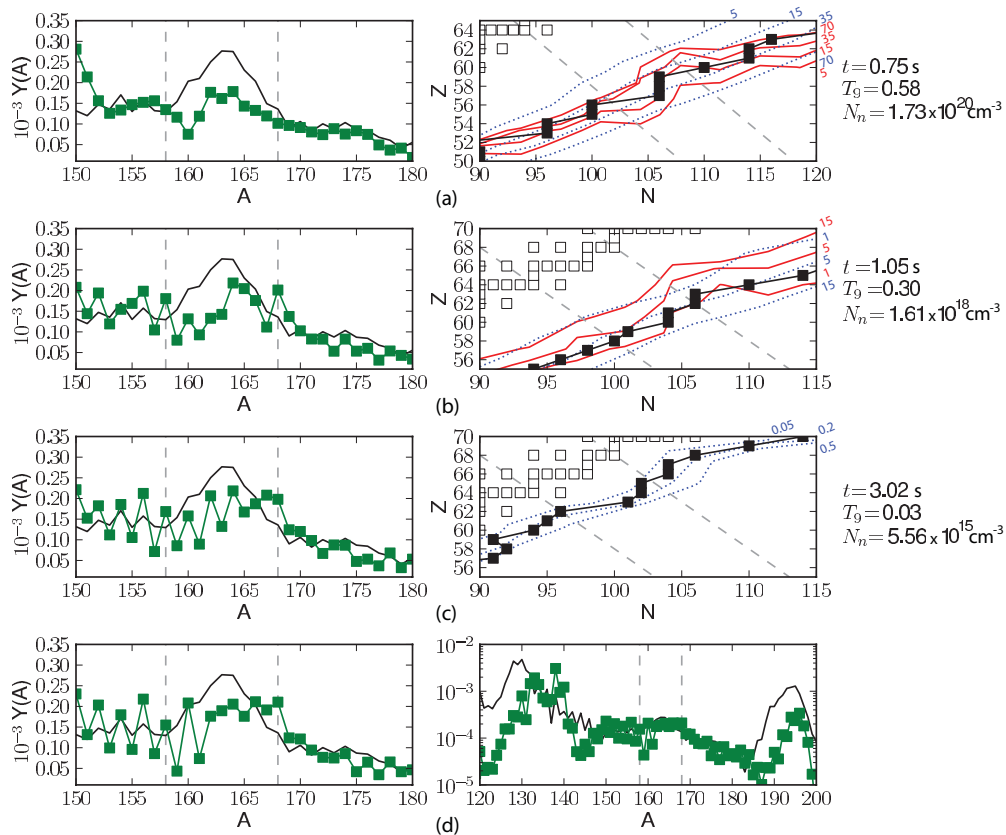


FIG. 7. (Color online) Neutron capture rates (solid red lines),  $\beta$ -decay rates (dotted blue lines),  $r$ -process path (filled squares in the right column), and abundance snapshots (left column) at (a) 20, (b) 15, and (c) 10 neutrons away from stability as the peak evolves during late times in a cold ETFSI-Q simulation. The rare-earth peak forms far from stability (a). However, it is washed out by the slow reduction in the structure of neutron capture rates of nuclei closer to stability (b). At 10 neutrons away from stability (c), the neutron capture rates are slower than the  $\beta$ -decay rates, so that only small changes to the abundance pattern occur after this point. Hence the disappearance of the lines of constant neutron capture rates in (c). Final abundances are shown in panel (d).

encounters structure in the neutron capture rates and this structure lasts until the point at which  $\beta$  decays take over neutron captures in the region ( $\tau_{ny}^{\text{REP}} \approx$  a few  $\tau_{\beta}^{\text{REP}}$ ).

A successful peak formation occurs in a hot evolution when the  $r$ -process path encounters a local deformation maximum, leading to a well-defined kink structure in the separation energies in the rare-earth region.

For a given nuclear model, the structure of neutron capture rates and the structure of the separation energies may not align in the  $NZ$  plane. This in turn can affect the timing and location of peak formation and hence the nuclei which are relevant.

Odd-even effects in the abundances can accumulate or persist through the decay back to stability, resulting in visible features in the final abundances. Smoothing of the abundances usually occurs in between neutron capture freeze-out ( $\tau_{ny}^{\text{REP}} = \tau_{\beta}^{\text{REP}}$ ) and the time in which  $\beta$  decays fully take over neutron captures in the region ( $\tau_{ny}^{\text{REP}} \approx$  a few  $\tau_{\beta}^{\text{REP}}$ ); however, this may not always happen.

We now discuss three different nuclear models in this context. Since separation energies vary among nuclear data we instead (for consistency) use  $\langle \delta N \rangle$ , the abundance-weighted average neutrons from stability, to measure the  $r$ -process path's progression.

Compared to the other nuclear models studied here, we find that simulations which use the FRDM nuclear data best match the solar data in the rare-earth peak region in both hot and cold evolutions. In fact, we find (in agreement with previous studies [40,42]) that the FRDM nuclear model is the only model to show a well-formed rare-earth peak consistently in the final abundance pattern.

Simulations with the FRDM nuclear data do not consistently form rare-earth peaks far from stability ( $\langle \delta N \rangle > 20$ ). Instead, peak formation ensues when the path is much closer, on average in between 15 and 20 neutrons away from stability. We can see the evolution of the peak region for a cold FRDM evolution in Fig. 5. At  $\langle \delta N \rangle \sim 20$ , panel (a), the structure in the capture rates has yet to manifest itself, resulting in relatively flat abundances. As the path moves back to stability,  $\langle \delta N \rangle \sim 15$ , panel (b), it encounters nuclei in the peak region with relatively slower neutron capture rates than the surrounding regions (note the bending in the red lines). These conditions persist all the way back to stability, resulting in a well-formed rare-earth peak. A similar scenario occurs in hot evolutions; see Fig. 6.

FRDM shows a slight overlap between neutron capture structure and separation energy structure. The structure in

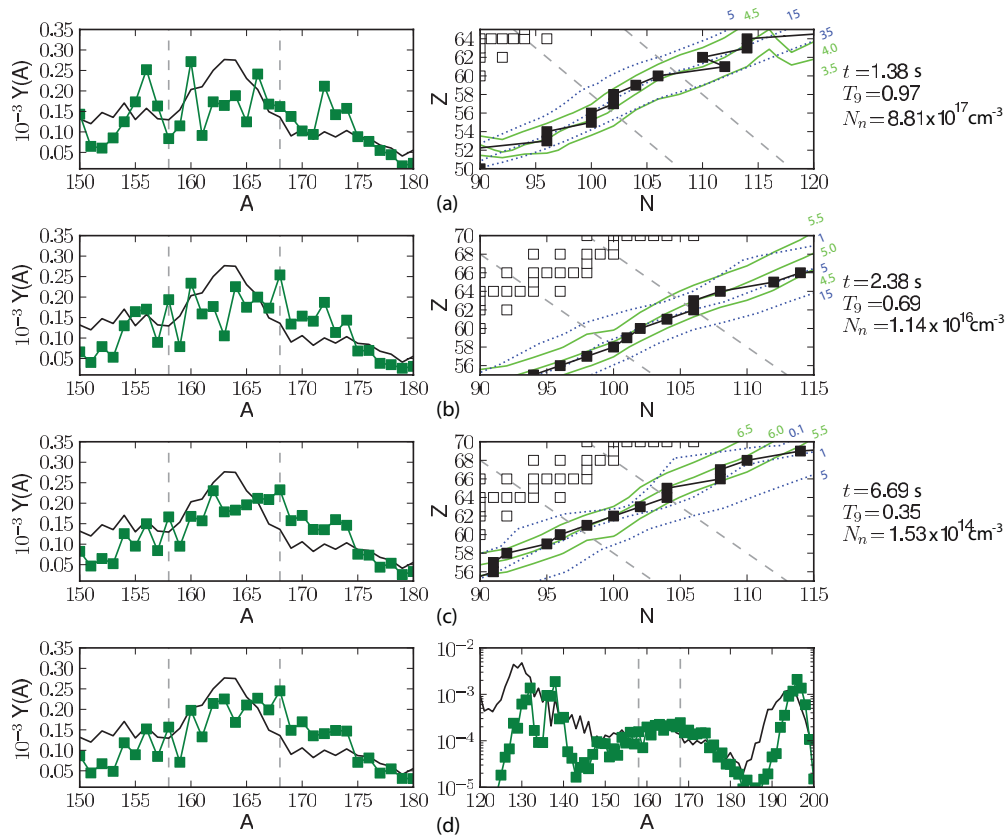


FIG. 8. (Color online) The rare-earth peak begins to form far from stability in this hot ETFSI-Q simulation (a) due to the separation energy kink structure beyond 20 neutrons from stability (not shown). However, it is washed out by the slow reduction in the kink structure of the separation energies of nuclei closer to stability (b). Separation energies (solid green lines),  $\beta$ -decay rates (dotted blue lines),  $r$ -process path (filled squares in the right column), and abundance snapshots (left column) are shown at (a) 20, (b) 15, and (c) 10 neutrons away from stability. Final abundances are shown in panel (d).

the separation energies occurs between  $\langle \delta N \rangle \sim 12$  and 20 and the structure in the capture rates occurs between  $\langle \delta N \rangle \sim 10$  and 15. This delays peak formation in cold scenarios until around 15 neutrons from stability, while hot evolutions typically begin peak formation approximately 20 neutrons from stability.

Simulations with the ETFSI-Q nuclear model consistently form a solar-like rare-earth peak far from the stable nuclei ( $\langle \delta N \rangle \gtrsim 20$ ). This is most apparent in colder simulations (see right panels of Fig. 4). However, this is not the end of the story as the material must decay back to stability. Figure 7 highlights this transition at an abundance-weighted average of  $\langle \delta N \rangle \sim 20$ , panel (a), 15, panel (b), and 10, panel (c), neutrons from stability. As the decay back to stability proceeds, the  $r$ -process path encounters nuclei whose neutron capture rates become homogeneous around the peak region. This slowly dissolves the structure, flattening the lines of constant neutron capture rates (compare top and middle panels). By the time the path is on average 15 neutrons away from stability the cold trapping mechanism cannot continue because neutron capture rates in the peak region are no longer slower than the surrounding regions. These conditions persist back to stability, resulting in a final abundance pattern with a more modest rare-earth peak.

Solar-like rare-earth peaks form far from the stable nuclei in ETFSI-Q models under hot evolutions as well. Far from stability, the structure (kink) in the separation energies results in the hot peak formation mechanism. Like the FRDM case, the separation energy kink in ETFSI-Q disappears as one moves closer to stability. However, the kink disappears while neutron captures are still dominant ( $\tau_{n\gamma}^{\text{REP}} \lesssim \tau_{\beta}^{\text{REP}}$ ) far from stability ( $\langle \delta N \rangle \geq 20$ ), resulting in a flattened final abundance distribution; see Fig. 8.

In this nuclear data set, the structure in the separation energies occurs farther from stability ( $\langle \delta N \rangle \geq 20$ ) than the structure seen in the neutron capture rates ( $\langle \delta N \rangle \sim 20$ ), influencing peak formation in a similar fashion to the FRDM case. The gross separation energy structure occurs very early on “before” the top panel of Fig. 8 and has already dissolved by  $\langle \delta N \rangle \sim 20$ .

Version 17 of the HFB nuclear model is optimized to over 2000 measured masses from [66], corresponding to a root mean square error of  $\lesssim 0.6$  MeV. This data set features detailed structure in the separation energies but little overall structure in the neutron capture rates. These features are reflected in our  $r$ -process abundances.

Figure 9 shows the decay back to stability of a cold  $r$ -process using HFB-17. At every snapshot, highlighting the

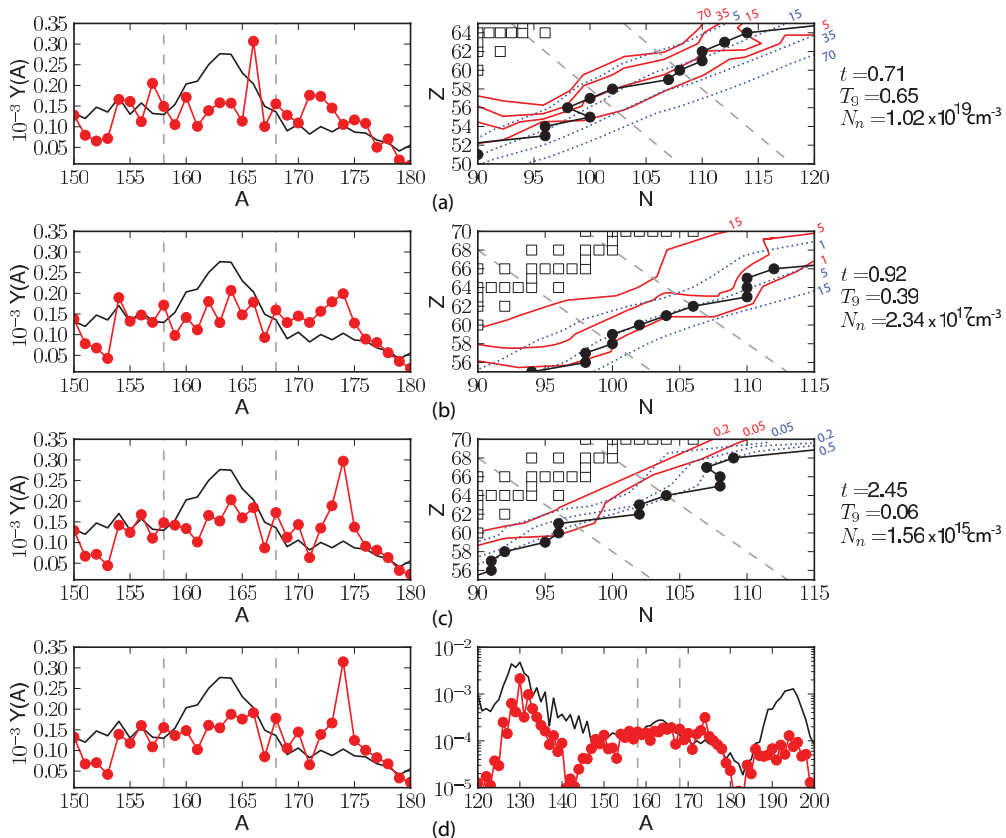


FIG. 9. (Color online) The final rare-earth peak (d) is relatively flat (as compared to the solar rare-earth peak) in this cold HFB-17 simulation. This occurs when the  $r$ -process path encounters a lack of neutron capture rate structure throughout the  $NZ$  plane in the peak region. Neutron capture rates (solid red lines),  $\beta$ -decay rates (dotted blue lines),  $r$ -process path (filled circles in the right column), and abundance snapshots (left column) are shown at (a) 20, (b) 15, and (c) 10 neutrons away from stability as in previous figures.

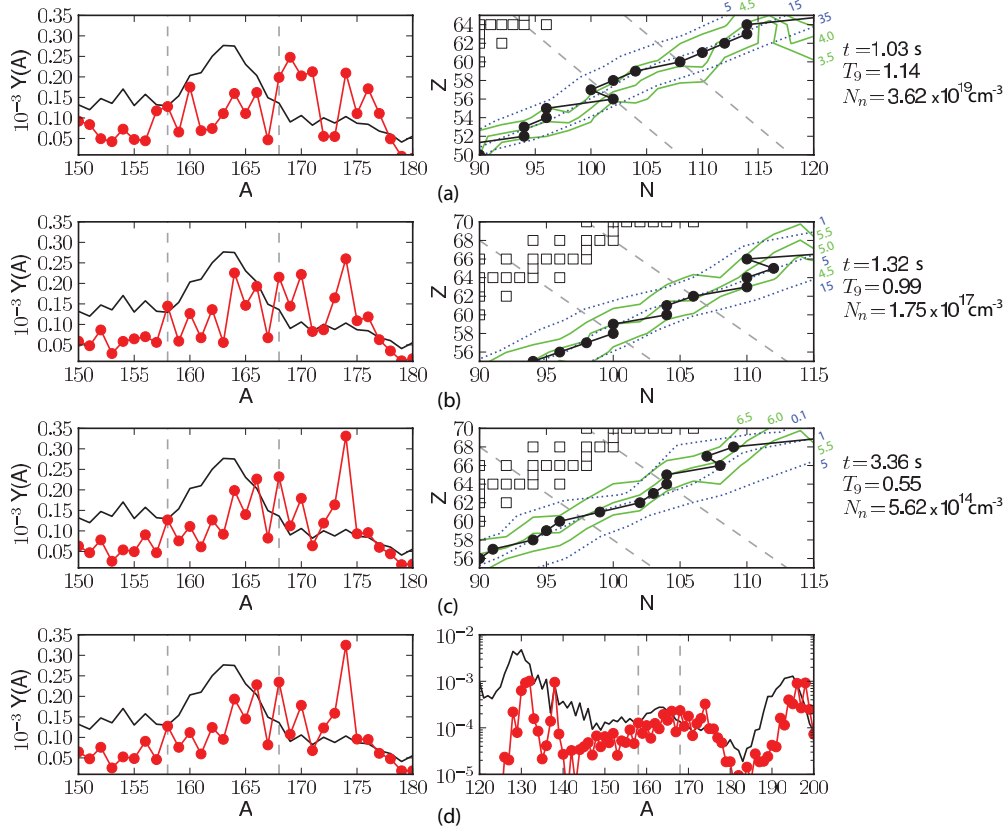


FIG. 10. (Color online) The final rare-earth peak (d) is relatively flat (as compared to the solar rare-earth peak) in this hot HFB-17 simulation. While there is detailed structure in the separation energies, there is little gross structure on the scale of the rare-earth peak. The slight abundance bump off-center of the actual peak region is due to the complex structure in the separation energies found off-center from the peak region. Separation energies (solid green lines),  $\beta$ -decay rates (dotted blue lines),  $r$ -process path (filled circles in the right column), and abundance snapshots (left column) are shown at (a) 20, (b) 15, and (c) 10 neutrons away from stability as in previous figures.

$r$ -process path's decay back to stability, we do not find the structure in the neutron capture rates as is found in the other two nuclear models. It is this relative homogeneity in the neutron capture rates throughout the rare-earth region which prevents the trapping mechanism from occurring in cold evolutions.

In hot  $r$ -process evolutions the situation is more intricate than for the corresponding cases of the other two nuclear models. The detailed structure in the separation energies results in a complex separation energy kink structure in the rare-earth region. However, due to the lack of gross structure as the separation energy increases (i.e., during the decay back to stability) the funneling mechanism cannot operate. This can be seen in Fig. 10 and illustrates the subtleties involved in forming the rare-earth peak.

In the above discussion we consider one hot and one cold evolution. In Fig. 11 we highlight astrophysical conditions which produce rare-earth peaks that best match the solar pattern. The shaded regions contain rare-earth peaks which fit the solar data better than a constant abundance,  $Y(A) = \text{constant}$ , matches the solar pattern. The hot peak formation mechanism operates between  $n \sim 2$  and  $n \sim 5$  while the cold peak formation mechanism operates above  $n \sim 5$ . Fission is included and operates for entropies above  $S = 200$  with

$Y_e = 0.30$  and above  $S = 300$  with  $Y_e = 0.40$ . These computations contain asymmetric fission using daughter products outlined by [67], resulting in one daughter product being proportionally heavier than the other.

The discussion in this section showcases the need for nuclear structure measurements far from stability. As we have seen, the nuclei that are important for rare-earth peak formation lie in between 10 and 20 neutrons away from stability. Furthermore, it is the nuclei which are the closest to stability, those in between 10 and 15 neutrons from stability, which are most influential to peak formation as they set or potentially dissolve the peak structure all together. In Fig. 12 we highlight these influential nuclei together with recent experimental mass measurements ([68,69]—green and [66]—gray) and known neutron capture rates ([70]—red).

## VI. SUMMARY AND CONCLUSIONS

We have studied the evolution of the rare-earth peak at late times (low neutron-to-seed ratio) under high-entropy ( $S > 100k_B$ )  $r$ -process conditions and offer new insight into its formation. To take into account uncertainties with nuclear

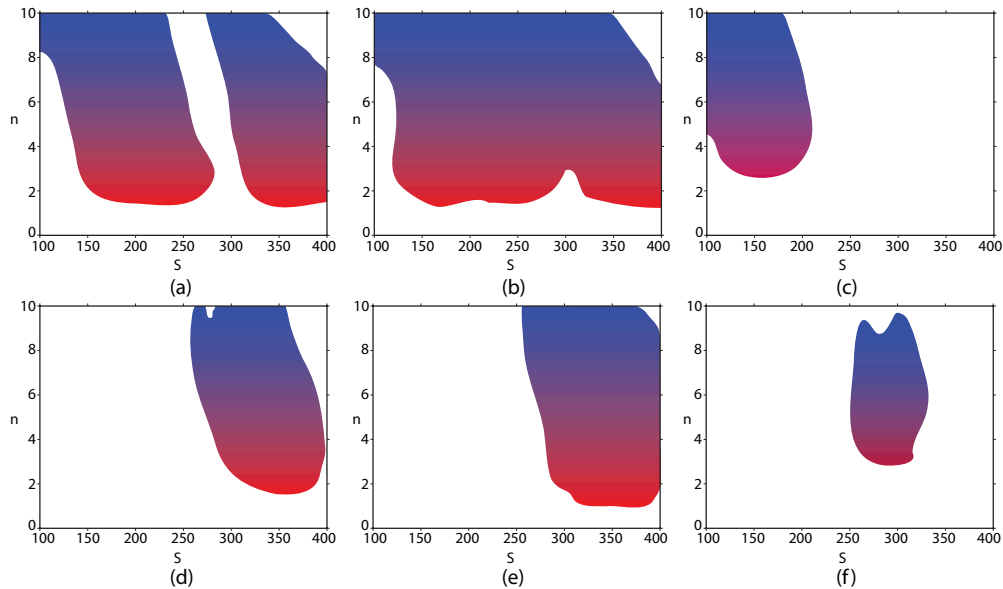


FIG. 11. (Color online) The regions which produce a rare-earth peak that best match the solar pattern. The hot rare-earth peak formation mechanism operates between  $n \sim 2$  and  $n \sim 5$ . The cold mechanism operates above  $n \sim 5$ . Panels (a), (b), and (c) have  $Y_e = 0.30$ . Panels (d), (e), and (f) have  $Y_e = 0.40$ . Columns correspond to the same nuclear data: ETFSI-Q (a) and (d), FRDM (b) and (e), and HFB-17 (c) and (f).

physics in the region our calculations employed three sets of nuclear data (FRDM, ETFSI-Q, and HFB-17).

Two late-time evolutions were considered: a hot  $r$ -process with temperatures high enough to support  $(n, \gamma) \rightleftharpoons (\gamma, n)$  equilibrium and a cold  $r$ -process with lower temperatures where there are no photodissociation flows, only competition between neutron captures and  $\beta$  decays after  $R = 1$ . By studying the late-time evolutions we show that development

of the rare-earth peak is strongly influenced by separation energies and neutron capture rates of nuclei in this region. The differences in late-time evolution (hot versus cold) determine which nuclear physics input is important (separation energies versus neutron capture rates, respectively) during the final stages of the  $r$ -process.

In hot evolutions the combination of photodissociation, neutron capture, and  $\beta$  decay results in a mechanism which funnels material into the peak region. A successful peak formation in hot evolutions is imprinted on the abundance pattern when the structure in the separation energies, the “kink,” is well defined *and* the  $r$ -process path crosses the kink region during the  $(n, \gamma) \rightleftharpoons (\gamma, n)$  freeze-out.

We contrast this with the peak formation mechanism which occurs in cold  $r$ -process environments. Here the important nuclear physics for peak formation lies in the local structure of the neutron capture rates. When the neutron capture rates are slow in the peak region relative to the surrounding regions (creating the characteristic “bow” in the lines of constant neutron capture rates) material can become trapped in the peak region, thus forming the peak. A successful peak formation in cold evolutions is imprinted on the abundance pattern when the structure in the neutron capture rates lasts until the point at which  $\beta$  decays take over neutron captures in the region ( $\tau_{n\gamma}^{\text{REP}} \approx \text{a few } \tau_{\beta}^{\text{REP}}$ ). Therefore, future studies of  $\beta$ -decay rates are warranted.

The rare-earth peak is extremely sensitive to the subtleties of nuclear physics input. Neutron capture is particularly important in both hot and cold evolutions. For instance, we find that neutron capture can play two competing roles in peak formation: it can be responsible for creating the peak, but it also can potentially dissolve the peak. Neutron capture rate structure and separation energy structure in the same nuclear model may not overlap in the  $NZ$  plane. This in turn can

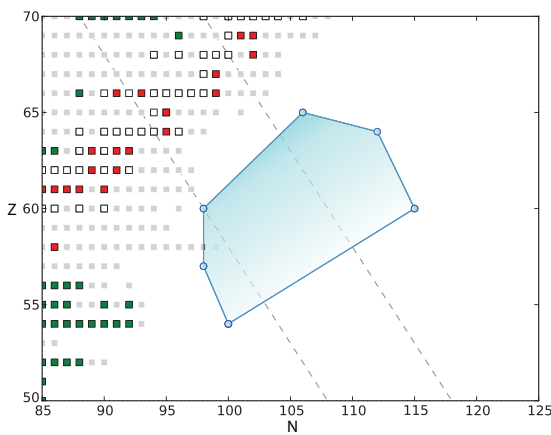


FIG. 12. (Color online) The nuclei which are important to rare-earth peak formation. The most influential nuclei are closer to stability in darker shading as they set or potentially dissolve the peak structure. Also shown is the current extent of experimental data for the rare-earth elements. Isotopes with measured masses in the AME2003 mass table are shaded in light gray. Recent ISOLTRAP and JFYLTRAP mass measurements are highlighted in green (dark gray in print version) and cross-section data from the online CSISRS database are highlighted in red (black in print version). Stable isotopes are shown by unfilled squares as in previous figures.

affect the timing and location of peak formation in different thermodynamic conditions.

We have shown that the rare-earth peak in principle offers unique insight into the late-time behavior of the  $r$ -process under high-entropy conditions because it forms away from the closed shells during freeze-out while material decays back to stability. Rare-earth peak formation is sensitive to the structure of separation energies and/or neutron capture rates about 10 to 15 neutrons away from the stable rare-earth peak. Future measurements at radioactive ion beam facilities could reach this important region and will be critical in placing constraints on nuclear models. This in turn will lead to improved  $r$ -process

predictions, allowing the rare-earth peak to evolve into a powerful tool for understanding the  $r$ -process.

#### ACKNOWLEDGMENTS

We thank A. Arcones and T. Rauscher for valuable discussions. We thank North Carolina State University for providing the high-performance computational resources necessary for this project. This work was supported in part by US Department of Energy Grants No. DE-FG02-02ER41216, No. DE-SC0004786, and No. DE-FG02-05ER41398.

- 
- [1] M. Arnould, S. Goriely, and K. Takahashi, *Phys. Rep.* **450**, 97 (2007).
- [2] Y.-Z. Qian and G. J. Wasserburg, *Phys. Rep.* **442**, 237 (2007), the Hans Bethe Centennial Volume 1906–2006.
- [3] D. Argast, M. Samland, F.-K. Thielemann, and Y.-Z. Qian, *Astron. Astrophys.* **416**, 997 (2004).
- [4] B. S. Meyer, G. J. Mathews, W. M. Howard, S. E. Woosley, and R. D. Hoffman, *Astrophys. J.* **399**, 656 (1992).
- [5] Y.-Z. Qian and S. E. Woosley, *Astrophys. J.* **471**, 331 (1996).
- [6] K. Sumiyoshi, H. Suzuki, K. Otsuki, M. Terasawa, and S. Yamada, *Publ. Astron. Soc. Jpn.* **52**, 601 (2000).
- [7] K. Otsuki, H. Tagoshi, T. Kajino, and S.-Y. Wanajo, *Astrophys. J.* **533**, 424 (2000).
- [8] T. A. Thompson, A. Burrows, and B. S. Meyer, *Astrophys. J.* **562**, 887 (2001).
- [9] Y.-Z. Qian, *Nucl. Phys. A* **752**, 550 (2005).
- [10] F.-K. Thielemann, A. Arcones, R. Käppeli, M. Liebendörfer, T. Rauscher, C. Winteler, C. Fröhlich, I. Dillmann, T. Fischer, G. Martínez-Pinedo, K. Langanke, K. Farouqi, K.-L. Kratz, I. Panov, and I. K. Korneev, *Prog. Part. Nucl. Phys.* **66**, 346 (2011).
- [11] A. Arcones, H.-T. Janka, and L. Scheck, *Astron. Astrophys.* **467**, 1227 (2007).
- [12] T. Fischer, S. C. Whitehouse, A. Mezzacappa, F.-K. Thielemann, and M. Liebendörfer, *Astron. Astrophys.* **517**, A80 (2010).
- [13] L. Hüdepohl, B. Müller, H. T. Janka, A. Marek, and G. G. Raffelt, *Phys. Rev. Lett.* **104**, 251101 (2010).
- [14] J. M. Lattimer, F. Mackie, D. G. Ravenhall, and D. N. Schramm, *Astrophys. J.* **213**, 225 (1977).
- [15] C. Freiburghaus, S. Rosswog, and F.-K. Thielemann, *Astrophys. J.* **525**, L121 (1999).
- [16] S. Goriely, P. Demetriou, H.-T. Janka, J. M. Pearson, and M. Samyn, *Nucl. Phys. A* **758**, 587 (2005).
- [17] R. Surman, G. C. McLaughlin, M. Ruffert, H.-T. Janka, and W. R. Hix, *Astrophys. J.* **679**, L117 (2008).
- [18] B. D. Metzger, G. Martínez-Pinedo, S. Darbha, E. Quataert, A. Arcones, D. Kasen, R. Thomas, P. Nugent, I. V. Panov, and N. T. Zinner, *Mon. Not. R. Astron. Soc.* **406**, 2650 (2010).
- [19] S. Goriely, A. Bauswein, and H.-T. Janka, *Astrophys. J. Lett.* **738**, L32 (2011).
- [20] S. Wanajo and H.-T. Janka, *Astrophys. J.* **746**, 180 (2012).
- [21] O. L. Caballero, G. C. McLaughlin, and R. Surman, *Astrophys. J.* **745**, 170 (2012).
- [22] R. Surman and G. C. McLaughlin, *Astrophys. J.* **603**, 611 (2004).
- [23] G. C. McLaughlin and R. Surman, *Nucl. Phys. A* **758**, 189 (2005).
- [24] R. Surman, G. C. McLaughlin, and W. R. Hix, *Astrophys. J.* **643**, 1057 (2006).
- [25] S. E. Woosley, D. H. Hartmann, R. D. Hoffman, and W. C. Haxton, *Astrophys. J.* **356**, 272 (1990).
- [26] P. Banerjee, W. C. Haxton, and Y. Z. Qian, *Phys. Rev. Lett.* **106**, 201104 (2011).
- [27] C. L. Fryer, F. Herwig, A. Hungerford, and F. X. Timmes, *Astrophys. J.* **646**, L131 (2006).
- [28] J. C. Wheeler, J. J. Cowan, and W. Hillebrandt, *Astrophys. J.* **493**, L101 (1998).
- [29] S. Wanajo, M. Tamamura, N. Itoh, K. Nomoto, Y. Ishimaru, T. C. Beers, and S. Nozawa, *Astrophys. J.* **593**, 968 (2003).
- [30] H. Ning, Y.-Z. Qian, and B. S. Meyer, *Astrophys. J.* **667**, L159 (2007).
- [31] P. T. Hosmer, H. Schatz, A. Aprahamian, O. Arndt, R. R. C. Clement, A. Estrade, K. L. Kratz, S. N. Liddick, P. F. Mantica, W. F. Mueller, F. Montes, A. C. Morton, M. Ouellette, E. Pellegrini, B. Pfeiffer, P. Reeder, P. Santi, M. Steiner, A. Stolz, B. E. Tomlin, W. B. Walters, and A. Wöhr, *Phys. Rev. Lett.* **94**, 112501 (2005).
- [32] K. J. Jones *et al.*, *AIP Conf. Ser.* **1098** 153 (2009).
- [33] P. Möller, J. R. Nix, W. D. Myers, and W. J. Swiatecki, *At. Data Nucl. Data Tables* **59**, 185 (1995).
- [34] J. M. Pearson, R. C. Nayak, and S. Goriely, *Phys. Lett. B* **387**, 455 (1996).
- [35] S. Goriely, N. Chamel, and J. M. Pearson, *Phys. Rev. Lett.* **102**, 152503 (2009).
- [36] E. M. Burbidge, G. R. Burbidge, W. A. Fowler, and F. Hoyle, *Rev. Mod. Phys.* **29**, 547 (1957).
- [37] Y.-Z. Qian, *Prog. Part. Nucl. Phys.* **50**, 153 (2003).
- [38] J. J. Cowan, F.-K. Thielemann, and J. W. Truran, *Phys. Rep.* **208**, 267 (1991).
- [39] C. Sneden, J. J. Cowan, and R. Gallino, *Annu. Rev. Astron. Astrophys.* **46**, 241 (2008).
- [40] R. Surman, J. Engel, J. R. Bennett, and B. S. Meyer, *Phys. Rev. Lett.* **79**, 1809 (1997).
- [41] M. Mumpower, G. C. McLaughlin, and R. Surman, *PoS, NIC-XI:273* (2010).
- [42] A. Arcones and G. Martínez-Pinedo, *Phys. Rev. C* **83**, 045809 (2011).
- [43] A. G. W. Cameron, *Publ. Astron. Soc. Pac.* **69**, 201 (1957).
- [44] D. N. Schramm and W. A. Fowler, *Nature (London)* **231**, 103 (1971).

- [45] K. Marti and H. D. Zeh, *Meteoritics* **20**, 311 (1985).
- [46] R. Surman and J. Engel, *Phys. Rev. C* **64**, 035801 (2001).
- [47] K. Otsuki, G. J. Mathews, and T. Kajino, *New Astron.* **8**, 767 (2003).
- [48] <http://www.frib.msu.edu>.
- [49] <http://www.gsi.de/portrait/fair.html>.
- [50] S. Wanajo, *Astrophys. J.* **666**, L77 (2007).
- [51] K. Farouqi, K.-L. Kratz, B. Pfeiffer, T. Rauscher, F.-K. Thielemann, and J. W. Truran, *Astrophys. J.* **712**, 1359 (2010).
- [52] J. Beun *et al.*, *J. Phys. G* **36**, 025201 (2009).
- [53] R. Surman, J. Beun, G. C. McLaughlin, and W. R. Hix, *Phys. Rev. C* **79**, 045809 (2009).
- [54] W. R. Hix and F.-K. Thielemann, *J. Comput. Appl. Math.* **109**, 321 (1999).
- [55] O. Schenk and K. Gärtner, *Future Gener. Comput. Syst.* **20**, 475 (2004).
- [56] B. S. Meyer, *Phys. Rev. Lett.* **89**, 231101 (2002).
- [57] I. V. Panov and H.-T. Janka, *Astron. Astrophys.* **494**, 829 (2009).
- [58] G. C. Mc Laughlin, J. M. Fetter, A. B. Balantekin, and G. M. Fuller, *Phys. Rev. C* **59**, 2873 (1999).
- [59] T. Rauscher and F.-K. Thielemann, *At. Data Nucl. Data Tables* **75**, 1 (2000).
- [60] T. Rauscher and F.-K. Thielemann, [arXiv:nucl-th/9802040](https://arxiv.org/abs/nucl-th/9802040).
- [61] <http://www.astro.ulb.ac.be/>.
- [62] S. Goriely, S. Hilaire, and A. J. Koning, *Astron. Astrophys.* **487**, 767 (2008).
- [63] <http://www.astro.ulb.ac.be/>.
- [64] P. Möller, B. Pfeiffer, and K. L. Kratz, *Phys. Rev. C* **67**, 055802 (2003).
- [65] C. Freiburghaus, J.-F. Rembges, T. Rauscher, E. Kolbe, F.-K. Thielemann, K.-L. Kratz, B. Pfeiffer, and J. J. Cowan, *Astrophys. J.* **516**, 381 (1999).
- [66] G. Audi, O. Bersillon, J. Blachot, and A. H. Wapstra, *Nucl. Phys. A* **729**, 3 (2003).
- [67] P. A. Seeger, W. A. Fowler, and D. D. Clayton, *Astrophys. J. Suppl.* **11**, 121 (1965).
- [68] <http://isoltrap.web.cern.ch>.
- [69] <https://www.jyu.fi/fysiikka/en/research/accelerator/igisol/trap>.
- [70] <http://www.nndc.bnl.gov/exfor>.
- [71] F. Kappeler, H. Beer, and K. Wisshak, *Rep. Prog. Phys.* **52**, 945 (1989).